Accepted manuscript. Published in Journal of Engineering Mechanics (2019). Version of record: https://doi.org/10.1061/(ASCE)EM.1943-7889.0001741. This material may be downloaded for personal use only. Any other use requires prior permission of the American Society of Civil Engineers. This material may be found at https://doi.org/10.1061/(ASCE)EM.1943-7889.0001741.

A constitutive theory for sand based on the concept of critical fabric surface

Yida Zhang[1], Xiang Zhou[2] and Yuxuan Wen[3]

ABSTRACT

A novel theoretical framework for the interpretation and modeling of the critical state behavior of granular soils is proposed in this paper. The theory is built upon the hypothesis that the fabric state of granular assemblies is attracted by a critical fabric surface under continuous shearing. A fabric ratio-stress ratio relation and a fabric-porosity relation are proposed based on recent Discrete Element Modeling (DEM) experimental results. It follows that the existence of a critical state line in the conventional *e-p-q* space can be derived by combining the above elements, offering a new perspective on the critical state phenomenon. Simple fabric evolution laws are proposed to capture the first-order features of the stress-strain-fabric behaviors of granular soils. The basic evolution laws are then enhanced to capture the behavior of natural sand. The computed results agree well with the data from Toyoura sand under a wide range of pressure and density conditions. This exploratory study reveals a promising pathway to integrate various microstructure information in the continuum modeling of granular soils. The generality and limitations of the model is also discussed at the end of this paper.

[1] Assistant Professor, Department of Civil, Environmental and Architectural Engineering, University of Colorado Boulder, 1111 Engineering Dr, Boulder, CO 80309. Corresponding Author. Email address: Yida.Zhang@Colorado.edu

[2] PhD candidate, Department of Civil, Environmental and Architectural Engineering, University of Colorado Boulder, 1111 Engineering Dr, Boulder, CO 80309.

[3] Graduate student, Department of Civil, Environmental and Architectural Engineering, University of Colorado Boulder, 1111 Engineering Dr, Boulder, CO 80309.

Key words: Critical state; Critical fabric surface; Fabric tensor; Coordination number; Soil Mechanics; Granular mechanics.

BACKGROUND

The Critical State Theory (CST) (Roscoe, Schofield and Wroth, 1958, Schofield and Wroth, 1968) is one of the most significant milestones in modern soil mechanics research. Central to the theory is the existence of a unique critical state line (CSL) in the void ratio *e*– mean stress *p*– deviatoric stress *q* space that attracts the state of soils subjected to shearing. Since 90's, many studies have showed that sands prepared to the same initial void ratio respond differently under different shearing modes (Mooney, Finno and Viggiani, 1998, Vaid and Thomas, 1995, Yoshimine, Ishihara and Vargas, 1998), leading to the debate of the uniqueness of the critical state and the significant impact of fabric anisotropy on the behavior of granular soils. Recently, Li and Dafalias (2012) proposed an appealing reconciliation between the classical CST and the experimentally observed non-unique CSLs. They stated that, in addition to the void ratio and stress ratio, the second-rank fabric tensor must also reach to its critical value at critical state, i.e.

$$q / p = M, e = e_c, \hat{F}_{ij} = \hat{F}_{ij}^c \tag{1}$$

where $\hat{F}_{ij}$ is the normalized deviatoric fabric tensor of the third kind (i.e. $\mathrm{tr}(\hat{F}_{ij}) = 0$). With this extended definition, the multiple apparent CSLs on the *e*-*p* plane can be explained as the intermediate states that do not satisfy $\hat{F}_{ij} = \hat{F}_{ij}^c$. Continuous shearing will eventually bring these pseudo CSLs into one unique CSL, which complies to the classical CST. Their theory does not constrain the definition of fabric tensors nor limit the form of constitutive laws. Therefore, it is regarded an extension of the original CST and referred to as the Anisotropic Critical State Theory (ACST). The development of ACST has led a new round of developments on fabric-based sand

models (Dafalias and Taiebat, 2016, Papadimitriou, Chaloulos and Dafalias, 2019, Tasiopoulou and Gerolymos, 2016, Zhao and Gao, 2015) and inspired numerous experimental studies enabled by Discrete Element Method (DEM) simulations (Fu and Dafalias, 2015, Zhao and Guo, 2013) and in-situ X-ray micro tomography (XCT) techniques (Imseeh, Druckrey and Alshibli, 2018, Wiebicke, Andò, Salvatore, Viggiani and Herle, 2017). These studies have produced a wealth of microscale information which may offer new possibilities for interpreting the macroscopic soil behaviors. Some of the latest experimental findings on critical state fabrics and fabric evolution are briefly reviewed herein, aiming to identify new links between critical state and microstructure of granular soils

REVIEW OF RECENT DEM RESULTS ON CRITICAL FABRIC

First of all, it is important to note that soil fabric is a general concept and its mathematical representation is not uniquely defined. In majority of the recent DEM works, granular microstructure has been represented by a second-order fabric tensor defined through either contact norms, void vectors, or the particle orientations (Kruyt, 2012, Nguyen, Rahman and Fourie, 2016, Shi and Guo, 2018, Wang and Wei, 2016, Yang and Wu, 2016, Zhao and Guo, 2013). No matter which type of fabric tensor is selected, Li and Dafalias (2015) pointed out that the adaptation of fabric tensor in continuum descriptions of sand must follow thermodynamic consistency. Fu and Dafalias (2011) and Wang, Fu, Zhang and Dafalias (2017) found that a unique state is reached for each of these three fabric tensor definitions, irrespective of the initial void ratio and the orientation and intensity of fabric anisotropy. Zhao and Guo (2013) conducted a series of true triaxial DEM tests and reported that the contact-based fabric tensor reaches a well-defined ultimate envelop at critical state, the shape of which is similar but reciprocal to the critical stress envelop in the deviatoric plane. They further demonstrated that the first joint invariant of the stress and fabric

62 tensors at critical state K_c is independent of Lode angle, leading to the proposal of a new critical
63 state line in the *K*-*e*-*p* space. Nguyen et al. (2016, 2018) conducted three-dimensional (3D) DEM
64 triaxial tests and showed that the deviatoric component of contact-based fabric tensor at critical
65 state is uniquely related to *p* and *e*. In addition, they found that coordination number *CN* at critical
66 state is only a function of *p* and independent of drainage conditions and consolidation methods.
67 Kruyt and Rothenburg (2014) through two-dimensional (2D) DEM studies demonstrated that *CN*
68 and contact-based fabric anisotropy *A* at critical state are functions of the interparticle friction and
69 confining pressure. When plotting these fabric states in the "fabric space" (i.e. *A* vs. *CN* plot), a
70 critical fabric line can be identified for the studied granular system (Fig. 1a). Inspired by this, one
71 can similarly replot the critical-state fabric data from Fu and Dafalias (2011) and Nguyen, Rahman
72 and Fourie (2018) in Figs 1b and c. A third axis corresponding to *p* is added to the *A* vs. *CN* plot
73 to represent the varying confining pressures. Again, a critical fabric line in the *A*-*CN*-*p* space which
74 collects all the ultimate fabric states after sufficient shearing can be identified. Such line exists for
75 both contact and particle-based fabric tensors as shown in Fig. 1b, and are independent of the
76 drainage condition and initial anisotropy of the specimen as shown in Fig. 1c. For general shear
77 paths, *A* may be replaced by tensorial fabric deviator such that the critical fabric line become a
78 critical fabric surface as presented in Zhao and Guo (2013).

79 Other than critical state itself, the evolution of fabrics with stress and strain before reaching critical
80 state is also of great research interest. Many recent DEM and in-situ XCT experiments have shown
81 that the fabric anisotropy for dense specimens reaches to a peak first and then decrease to steady
82 state during shearing, similar to the *q*/*p* vs. ε_a plots (Fu and Dafalias, 2015, Imseeh, Druckrey and
83 Alshibli, 2018, Kruyt, 2012, Kruyt and Rothenburg, 2014, Shi and Guo, 2018, Thornton and Zhang,
84 2010, Yan and Zhang, 2013, Yang and Wu, 2016). This implies some correlations between fabric

anisotropy and stress ratio. Oda (1972a,b), to the authors' knowledge, presented the first attempt to establish such relation through observing sections of resin impregnated sand specimens. He proposed a fabric measure based on the projection of grain-to-grain contact areas on the Cartesian planes (S_x, S_y, and S_z). The measured stress ratio and fabric ratio shows an astonishing linear relationship (Fig. 2a). Thornton and Zhang (2010) plotted the stress envelop and the envelop for total-contact-based fabric tensor on the deviatoric plane, showing that both envelops monotonically enlarge while maintain a similar but reciprocal shape upon shearing. After separating the overall contact network into strong and weak contact sub-networks following Radjai, Jean, Moreau and Roux (1996), they found that the fabric envelope of the strong contacts exhibits an almost identical shape with the stress envelop, in contrary to the reciprocal shape of the envelop of the total-contact fabric. This phenomenon has been further investigated by Shi and Guo (2018). They observed a nonlinear, Lode-angle-dependent and pressure-dependent relation between stress ratio and the total-contact fabric ratio (which will be simply referred to as the fabric-stress relation hereafter) as shown in Fig. 2b. After screening out the weak contacts, a linear fabric-stress relation with a slope of nearly 1:1 appears (Fig. 2c):

$$\frac{q}{p} = \frac{\hat{G}_q^s}{\hat{G}_p^s} \tag{2}$$

where $\hat{G}_{ij}$ is normalized fabric tensor of the first kind, the relation of which with $\hat{F}_{ij}$ will be revealed in the next session; $\hat{G}_p = 1$ and $\hat{G}_q$ are the mean and deviatoric part of $\hat{G}_{ij}$, respectively; superscript 's' denotes strong-contact network. Their results suggested that this relation is independent of the shearing mode and confining pressure. Again, the strong-contact fabric and stress envelopes at critical state are observed to have the same shape on the deviatoric plane (Fig. 2d).

Based on the above review, it is possible to see some sort of unifications to the various CSLs defined in the conventional *e*-*p*-*q* space (as in CST), the *e*-*p*-*q*-F_{ij} space (as in ACST), and the *K*-*e*-*p* space (as in Zhao and Guo (2013)). In fact, the existence of a critical stress envelop (the first condition in Eq. (1)) is guaranteed if one combines the fabric-stress relation Eq. (2) together with the observed critical fabric envelop in Fig. 2d. In other words, a soil specimen will reach to a constant fabric state after enough shearing, at the same time it must reach a stationary stress state such that no further structural change is triggered. On the other hand, since void ratio is just one way to describe the packing efficiency of the granular assembly, it is plausible to assume that the pair of fabric descriptors CN and $\hat{G}_{ij}^{s}$ contain the same information as the void ratio does (i.e. a fabric-porosity relation exists). Combining this relation with the critical fabric surface in the $\hat{G}_{ij}^{s}$-CN-p space help to recover the other two conditions in Eq. (1). In summary, the above analysis suggests that the critical state of granular soils can be studied by exploiting a critical fabric surface complemented by a fabric-stress relation and a fabric-porosity relation. This offers a new viewpoint alternative to the ACST about the critical state phenomenon of sand and may enable structurally more convenient constitutive models to incorporate fabric effects. The goal of this paper is to exercise this philosophy and to integrate some of the above DEM findings in a new constitutive framework for granular soils. The remainder of this paper is organized as follows. First, a critical fabric surface is proposed with reference to the existing DEM data; This is followed by the development of a fabric-porosity relation which leads to a CSL expression in the *e*-*p* space; A fabric-stress relation is then proposed which gives the yield surface in the stress space; The section following specifies a simple fabric evolution law that satisfies the asymptotic requirements; Section 'Model Performance' shows the results of the basic model under monotonic and cyclic loading in different drainage conditions and the corresponding fabric evolutions; This model is

130 then enhanced to quantitatively capture the experimental data from Toyoura sands; The last
131 section concludes the current study and discusses the limitations and future works.

132 **CRITICAL FABRIC SURFACE**

133 Just like CST or ACST, the definition of fabric tensor is not provided by the current theory and it
134 can be chosen based on specific modeling purposes. The previous review identified several
135 appealing properties possessed by the fabric tensor defined on strong contacts: (1) its second
136 invariant exhibits a simple linear relation with the stress ratio which is independent of Lode angle
137 and confining pressure (Fig. 2c) and (2) the shape of its critical envelop on the deviatoric plane is
138 similar to the critical stress envelop (Fig. 2d). Therefore, the strong-contact fabric tensor is a
139 natural choice for the current development aiming to demonstrate the basic concept of critical
140 fabric surface and to establish a constitutive theory pertained to this concept. In the following, all
141 fabric components are defined on strong contacts and the superscript '*s*' denoting strong-contact
142 as in Eq. (2) will be dropped for conciseness. The generality of theory for other fabric definitions
143 will be discussed in the last section of this paper.

144 The fabric tensors of the first, second and third kind for the current theory are defined as follows.
145 Consider the following directional distribution:

146 $$\rho(\mathbf{n}) = \frac{2N_c^s}{N_p}\hat{\rho}_c^s(\mathbf{n}) = \Delta\hat{\rho}_c^s(\mathbf{n}) \tag{3}$$

147 where $\hat{\rho}_c^s(\mathbf{n})$ is the distribution density of strong contacts which is defined by $f_n > \langle f_n \rangle$ with f_n
148 the normal contact force and $\langle f_n \rangle$ the average contact force (Radjai, Jean, Moreau and Roux,
149 1996); N_p is the number of particles in the assembly; N_c^s is the number of strong contacts; n_i is the
150 contact normal vector; the sum is over all contacts c in the strong contact network C^s. It follows

that $\Delta = \int_{4\pi} \rho(\mathbf{n}) d\Omega = \frac{2N_c^s}{N_p}$ represents the average strong contacts per particle (or the strong-contact coordination number) Here $\Omega \in [0, 4\pi]$ is the solid angle. It is possible to approximate Eq. (3) by a second-order tensor:

$$\rho(\mathbf{n}) \approx \frac{1}{4\pi} E_{ij} n_i n_j \tag{4}$$

where E_{ij}^s is the *fabric tensor of the second kind* (Kanatani, 1984) . It can be shown that $\Delta = \frac{1}{3} E_{kk}$ by integrating Eq. (4) over all directions. Multiplying Eq. (4) with $n_k n_l$ and integrate over $[0, 4\pi]$ gives:

$$E_{ij} = \frac{15}{2}\left(G_{ij} - \frac{1}{5}\Delta\delta_{ij} \right) \tag{5}$$

where G_{ij} is the fabric tensor of the first kind defined as

$$G_{ij} = \int_{4\pi} \rho(\mathbf{n}) n_i n_j d\Omega \tag{6}$$

with $G_{kk} = \Delta$. The deviator of E_{ij} can be expressed as:

$$F_{ij} = E_{ij} - \frac{1}{3} E_{kk}\delta_{ij} = \frac{15}{2}\left(G_{ij} - \frac{1}{3}\Delta\delta_{ij} \right) \tag{7}$$

which is called the *fabric tensor of the third kind*. Substituting Eq. (7) into (4) gives

$$\rho(\mathbf{n}) \approx \frac{1}{4\pi}\left(\Delta + F_{ij} n_i n_j \right) \tag{8}$$

which can be viewed as the spherical harmonic expansion of $\rho(\mathbf{n})$ truncated to the second order (Kanatani, 1984). It should be noted that all three fabric tensors have been used to approximate the

167 directional statistics in the granular literatures. The advantage of G_{ij} is that it can be easily
168 computed when then distribution $\rho(\mathbf{n})$ is known (via Eq. (6)); E_{ij} is convenient when the goal is
169 to map fabric tensors back to distributions (via Eq. (4)); F_{ij} is the deviator of E_{ij} which is a zero-
170 trace tensor. The three fabric tensors are interrelated through Eqs. (5) and (7), thus they are
171 equivalent in representing of soil fabric data. The normalized fabric tensors can be correspondingly
172 defined as

173 $$\hat{E}_{ij} = E_{ij} / \Delta \;;\; \hat{G}_{ij} = G_{ij} / \Delta \;; \hat{F}_{ij} = F_{ij} / \Delta \tag{9}$$

174 The core of the proposed theory is a critical fabric surface that attracts all fabric states upon
175 shearing. Noticing the similarity between the shapes of the critical fabric and stress surfaces on the
176 deviatoric plane (Fig. 2d), the former may be represented by adopting a common expression for
177 the deviatoric yield surface (Dafalias and Manzari, 2004):

178 $$F_{ij}^c = \hat{F}_{ij}^c \Delta = \sqrt{\frac{2}{3}} \hat{F}_c \Delta g(\theta) n_{ij} \;\text{ with }\; g(\theta) = \frac{2r}{(1+r) - (1-r)\cos 3\theta} \tag{10}$$

179 where g is an interpolation function accounting for the Lode-angle dependency; $n_{ij} = F_{ij} / \left\| F_{ij} \right\|$ is a
180 directional tensor that satisfies $n_{ii}=0$ and $n_{ij}n_{ij}=1$; θ is the Lode angle varies from 0 to $\pi/3$ defined
181 by $\cos(3\theta) = \sqrt{6} n_{ij} n_{jk} n_{ki}$; $\hat{F}_c$ and r are model parameters controlling the size and shape of the
182 deviatoric critical fabric surface, respectively. Fig. 3a visualizes Eq. (10) in the principal fabric
183 space. In the current model, there are no rules to prevent the fabric state lies outside of the critical
184 fabric surface. Radjai, Delenne, Azéma and Roux (2012) showed that spherical assemblies must
185 have some geometrical limitations that divides accessible and inaccessible fabric states. This
186 indicates there is a *bounding fabric surface* beyond which the skeleton structure would be unstable.

187 It is worth to explore such limitation for natural soils and its relationship with the critical fabric
188 surface in future studies.

189 Nguyen, Rahman and Fourie (2018) showed that the *CN* vs. *p* data at critical state can be fitted by
190 a power law equation. Similar expression may be adopted for the strong-contact coordination
191 number:

192 $$\Delta_c = \Delta_{c0} + h_c \left(\frac{p}{p_a} \right)^{\xi} \tag{11}$$

193 where Δ_{c0}, h_c and ξ are material parameters; p_a is the atmosphere pressure. Using Eq. (11) and the
194 definition of deviatoric fabric $F = \sqrt{3/2 F_{ij} F_{ij}}$, a critical fabric line can be plotted in the Δ-*F*-*p*
195 space (Fig. 3b). It is clear that $\hat{F}_c$ represents the slope of this line projected on the Δ-*F* plane. Fig.
196 3c plots the critical fabric states in the Δ-$\hat{F}$-*p* space to show its similarity with the experimental
197 data in Figs. 1b and c.

198 **FABRIC-POROSITY RELATION**

199 There exists several *CN*-ϕ models in granular physics, powder technology and chemical
200 engineering literatures (Calvetti, Combe and Lanier, 1997, Dodds, 1980, German, 2014, O'hern,
201 Silbert, Liu and Nagel, 2003, Ouchiyama and Tanaka, 1984, Rice, 1993, Suzuki, Kada and Hirota,
202 1999). Among them, the equation proposed by O'hern, Silbert, Liu and Nagel (2003) is found to
203 be quite versatile

204 $$CN - CN_0 = h_0 \left(\phi_0 - \phi \right)^{\varsigma} \tag{12}$$

205 where, h_0 and ζ are material parameters; CN_0 is the coordination number at a reference ϕ_0 porosity
206 which is usually taken at the jamming point. Fig. 4 shows the performance of Eq. (12) in capturing

a variety of *CN*-ϕ data for monotonic and polydisperse assemblies. It is worth to note that these data are obtained under isotropic compression condition. The evolution of *CN* subjected to both compression and shear is not very well understood at this moment. Limited DEM simulations showed that *CN* evolves with both volumetric and shear strains, implying that ϕ may be a function of both *CN* and fabric anisotropy (Kruyt, 2012). The authors are currently conducting a series of DEM experiments to further study this issue. Here Eq. (12) is tentatively accepted as the basis to develop a Δ-ϕ relation to close the model. Note that Δ contains only the coordination information of the strong contact network. Without further DEM data, it is assumed that porosity is related to Δ in a similar way as to *CN* considering the strong network is a subset of the total contact network. A Δ-ϕ relation in the same form as Eq. (12) is therefore proposed:

$$\Delta - \Delta_0 = h_0 \left(\phi_0 - \phi\right)^{\zeta} \tag{13}$$

where h_0 and ζ must be recalibrated based on the Δ-ϕ data; Δ_0 is the strong-contact coordination number corresponds to a reference porosity ϕ_0. We suggest to take ϕ_0 as the maximum porosity of the granular assembly at p=0 to ensure that Eq. (13) always gives a real positive value of Δ for all the accessible porosity values.

Combining Eqs. (13) and (11) gives the critical state line in the classical *e*-*p* space:

$$\phi_0 - \phi_c = \left(\frac{\Delta_{c0} - \Delta_0}{h_0} + \frac{h_c}{h_0} \left(\frac{p}{p_a} \right)^{\xi} \right)^{\frac{1}{\zeta}} \tag{14}$$

where $\phi_c = e_c / (1 + e_c)$; e_c is the critical void ratio. Fig. 5 compares Eq. (14), the CSL equation by Li and Wang (1998) and the critical state data by Verdugo and Ishihara (1996). Both models well capture the experimental data. Eq. (14) contains more parameter than Li and Wang's equation.

However, these parameters should not be viewed as redundant fitting parameters as each of them has a unique role in representing the $\Delta_c - p$ and the $\Delta - \phi$ relations for the granular material at concern. In other words, for the current model, critical state line in the *e-p-q* space is a derived property as the mean fabric Δ approaching to Δ_c rather than the other way around. This features an important difference between the current theory and the classical critical state models.

FABRIC-STRESS RELATION

The fabric-stress relation is responsible for mapping a fabric ratio to a stress ratio in the proposed model. Considering definition

$$\hat{G}_p = \frac{1}{3}; \hat{G}_q = \sqrt{\frac{3}{2}\hat{G}'_{ij}\,\hat{G}'_{ij}} \tag{15}$$

where $\hat{G}'_{ij} = \hat{G}_{ij} - \frac{1}{3}\delta_{ij}$ is the deviator of $\hat{G}_{ij}$, Eq. (2) can be written in general tensorial form:

$$\frac{s_{ij}}{p} = 3\hat{G}'_{ij} = 3\left(\frac{G_{ij}}{\Delta} - \frac{1}{3}\delta_{ij}\right) \tag{16}$$

Substituting Eqs. (7) and (9) into Eq. (16) gives the fabric-stress relation in terms of F_{ij}:

$$\frac{s_{ij}}{p} = \frac{2}{5}\frac{F_{ij}}{\Delta} \tag{17}$$

It is desirable to cast the model in a mathematical structure similar to the conventional elastoplastic framework. For this purpose, we relax this relation by allowing a small elastic regime surrounding the mapped fabric state. Specifically, Eq. (17) may be replaced by the following relation:

$$\left\| \frac{s_{ij}}{p} - \frac{2}{5}\frac{F_{ij}}{\Delta} \right\| \le \sqrt{\frac{2}{3}}m \tag{18}$$

where m is a small material constant; $\|\bullet\|$ is the Euclidean norm. Eq. (18) becomes identical to Eq. (17) if m is set to zero. The advantage of Eq. (18) is that it introduces a yield surface in the stress space that permits the utilization of elastoplasticity tools in model development. Such elastic regime is also physically plausible in representing soil responses subjected to small strain perturbations. Introducing

$$\alpha_{ij} = \frac{2}{5}\frac{F_{ij}}{\Delta} \tag{19}$$

, Eq. (18) can be rewritten in the form of a yield criterion:

$$y = \sqrt{\left(s_{ij} - p\alpha_{ij}\right)\left(s_{ij} - p\alpha_{ij}\right)} - \sqrt{\frac{2}{3}}mp \le 0 \tag{20}$$

Eq. (20) is a narrow cone that points towards the origin in the principal stress space. Geometrically, α_{ij} is the center of the yield surface on the π-plane and is usually referred as *back stress* in elastoplastic models; m defines the size of the yield surface in the deviatoric plane. The yield surface Eq. (20) is identical to the one proposed by Dafalias and Manzari (2004). The difference is that Eq. (20) is derived by relaxing the experimentally observed fabric-stress relationship rather than proposed a priori. Another conceptual difference is that the back stress α_{ij} in the current model is not an internal state variable (ISV) and does not have a separate evolution law. Its value should be computed from the F_{ij} and Δ according to Eq. (19).

Figs. 6a and b plot the critical fabric surface and its corresponding stress surface on the deviatoric plane, respectively. An arbitrary fabric state A in Fig. 6a is mapped on to the stress space in Fig. 6b as A' through Eq. (19). The yield surface Eq. (20) is a circle centered at point A' with radius $\sqrt{2/3}m$. Stress state can travel in this regime without causing microstructural changes, while

exceeding such limit will cause evolution of $\hat{F}_{ij}$ and hence a kinematic hardening of yield surface compatible to this load increment. Fig. 7 plots the modeled critical fabric and stress surfaces in the deviatoric planes of $\hat{G}'^{c}_{ij}$ and s^{c}_{ij} together with the data from Shi and Guo (2018). An excellent agreement is observed. Here $\hat{F}_{ij}$ is converted to $\hat{G}'_{ij}$ using Eq. (7).

FABRIC EVOLUTION LAW

The evolution of F_{ij} and Δ with respect to shear straining is the last component to close the model. First, it is noted that the Δ-ϕ relation already asserted some sort of linkage between Δ and the volumetric strain of the REV. Specifically, Eq. (13) can be rewritten in incremental form as

$$d\Delta = h_0\zeta\left(\phi_0 - \phi\right)^{\zeta-1}(-d\phi) = h_0\zeta\left(\phi_0 - \phi\right)^{\zeta-1} d\varepsilon_v \tag{21}$$

where $\varepsilon_v = \varepsilon_{kk}$ is the volumetric strain. Substituting additive decomposition $d\varepsilon_v = d\varepsilon_v^e + d\varepsilon_v^p$ into Eq. (21) leads to a similar decomposition of Δ:

$$d\Delta = d\Delta^e + d\Delta^p \tag{22}$$

with

$$d\Delta^e = \left(\frac{\partial\varepsilon_v}{\partial\Delta}\right)^{-1} d\varepsilon_v^e;\ d\Delta^p = \left(\frac{\partial\varepsilon_v}{\partial\Delta}\right)^{-1} d\varepsilon_v^p \tag{23}$$

where

$$\frac{d\varepsilon_v}{d\Delta} = \frac{1}{h_0\zeta\left(\phi_0 - \phi\right)^{\zeta-1}} = \frac{1}{h_0\zeta}\left(\frac{\Delta - \Delta_0}{h_0}\right)^{-\frac{\zeta-1}{\zeta}} \tag{24}$$

and superscripts 'e' and 'p' denotes elastic and plastic parts, respectively. The first equation of Eq. (23) indicates that the evolution of Δ^e is completely defined by the elastic model. Here, the

hypoelastic model used in Dafalias and Manzari (2004) and Li and Dafalias (2012) is adopted for simplicity. The elastic stiffness tensor is given by:

$$D^e_{ijkl} = \left(K - \frac{2}{3} G \right) \delta_{ij} \delta_{kl} + G \left(\delta_{ki} \delta_{lj} + \delta_{li} \delta_{kj} \right) \tag{25}$$

where

$$G = G_0 \frac{\left(2.97 - e\right)^2}{1+e} \sqrt{p p_a} \; ; \; K = G \frac{2\left(1+\nu\right)}{3\left(1-2\nu\right)} \tag{26}$$

; K and G are the bulk and shear modulus, respectively; ν, p_a and G_0 are the Poisson's ratio, atmosphere pressure and reference shear modules, respectively. It is straightforward to introduce fabric-dependency in the elastic model as shown by Cowin (1985) and Zhao and Gao (2015). However, to avoid obscuring the interpretation of the behavior of this basic model, the isotropic one described by Eq. (25) is used in generating the results.

On the other hand, the evolution of Δ^p must be proposed based on experimental observations. The goal here is to capture the asymptotic behavior rather than the full features of the Δ evolution. The simplest evolution law that allow Δ marching towards its critical value Δ_c is the following:

$$d\Delta^p = \lambda a \left(\Delta_c - \Delta \right) \tag{27}$$

where a is a material parameter governing the speed of Δ evolution; λ is the plastic multiplier which is equivalent to plastic shear strain. At critical state (i.e. $\Delta = \Delta_c, p = p_c$), Eq. (27) gives $d\Delta^p = 0$ and the elastic relation gives $d\Delta^e = 0$, thus the classical critical state condition $d\phi = 0$ is reached through Eq. (13).

It is well recognized that granular soils exhibit a contractive tendency at the beginning of shearing regardless of its initial density. To account for such initial contraction, it is necessary to introduce an increase in Δ^p that overcomes the attractor $\left(\Delta_c - \Delta\right)$ at the initial shearing stage. This can be realized by replacing Eq. (27) by following evolution law:

$$d\Delta^p = \lambda\left[a\left(\Delta_c - \Delta\right) + c\left\|F_{ij}^c - F_{ij}\right\|\right] \tag{28}$$

where c is a material constant that controls the magnitude of initial contraction. The second term on the right hand side of Eq. (28) measures the distance between the current fabric deviator to its corresponding critical value given by Eq. (10). This term vanishes as F_{ij} approaching F_{ij}^c, reducing Eq. (28) to Eq. (27). At the beginning of shearing, the second term contributes to a positive increment on Δ^p which can account for the initial contraction phenomenon. Since Eq. (27) is the special case of Eq. (28) at c=0, the latter will be used for model implementation for flexibility. Note that this model does not have an evolution law for the plastic volumetric strain. It should be instead computed by inverting Eq. (23):

$$d\varepsilon_v^p = \left(\frac{\partial \varepsilon_v}{\partial \Delta}\right) d\Delta^p \tag{29}$$

The evolution of F_{ij} directly governs the kinematic hardening of the model through Eq. (18). Again, the focus here is to match the asymptotic behavior and leave the secondary features for later developments. At large shear strains, F_{ij} converges to F_{ij}^c which can be described by a function similar to Eq. (27):

$$dF_{ij} = \lambda b\left(F_{ij}^c - F_{ij}\right) \tag{30}$$

where b is a material parameter that controls the rate of such convergence. Unlike the mean fabric Δ, the evolution of F_{ij} does not have to be decomposed into elastic and plastic parts because there is no such a total-from relation like Eq. (13) that links F_{ij} and the total strain. In addition, elastic shear strain only takes a few percentage of the total shear strain especially for samples arrives at critical states ($\varepsilon_s \approx 50\%$). Therefore, the evolution of F_{ij} here (Eq. (30)) is proposed to be solely driven by the plastic shear strain via λ for simplicity. This is equivalent to assume that elastic straining does not introduce fabric anisotropy, which may be a subject of further study for small-strain applications. To keep the model simple, the increment of plastic strain deviator is proposed to be normal to the deviatoric yield surface with a magnitude of λ:

$$de_{ij}^{p} = \lambda \frac{s_{ij} / p - \alpha_{ij}}{\left\| s_{ij} / p - \alpha_{ij} \right\|} \tag{31}$$

where $e_{ij} = \varepsilon_{ij} - \frac{1}{3}\varepsilon_{kk}$ is the strain deviator.

MODEL PERFORMANCE

The model response is examined here in triaxial space. The corresponding constitutive equations are summarized in Table 1. Here $\eta = q / p$ is the fabric ratio; $\varepsilon_s = \sqrt{2/3 e_{ij} e_{ij}}$ is the deviatoric strain; $\mathrm{sgn}(\cdot)$ is the sign function. All simulations in this section are conducted with critical state parameters calibrated in Fig. 6 together with $\hat{F}_c = 3$, elastic parameters G_0=125 and ν=0.05, yield parameter m=0.01, and evolution parameters a=10, b=50. Parameter c varies in different simulations.

Fig. 8 plots the model response under drained triaxial compression with different initial void ratio using c=0 (or Eq. (27)) and c=1.0. For qualitative comparison, Fig. 9 shows the DEM results by

339 Rothenburg and Kruyt (2004) on same test. It is observed that the model can capture the main
340 characteristics of drained behavior of sand, including 1) density-dependent stress-strain behaviors
341 (i.e. hardening for loose sand and softening for dense sand, Fig. 8a), 2) density-dependent
342 volumetric response (i.e. contraction for loose and dilation for dense sand, Fig. 8c) and 3) the
343 convergence of void ratio to a unique critical state line in the *e-p* space (Fig. 8c).

344 Comparing Figs 8d and e with Figs 9b and c, the model also successfully captures the main traits
345 of the evolution of coordination number and fabric anisotropy. Specifically, the model correctly
346 predicted that fabric anisotropy for dense specimens reaches to a peak first before reaching to its
347 critical value, which agrees well with other DEM and experimental results (Imseeh, Druckrey and
348 Alshibli, 2018, Shi and Guo, 2018). The effect of parameter c can be observed by comparing the
349 dashed line and the solid line in Figs 8c and d. As expected, adding this coefficient will allow the
350 model to predict an initial contraction upon shearing even for initially dense specimens. As F
351 approaches to F_c, such contractive trend diminishes and the curves for c=0 and c=1 converge to
352 each other. Fig. 8f shows that this model correctly implemented our hypothesis that soil's fabric
353 state is attracted by its critical fabric surface. Fabric states are allowed to exceed such surface in
354 order to capture the peak F for dense specimens. This feature is granted by Eq. (30) where the
355 asymptotic value F_{ij}^c is density-dependent according to Eq. (10).

356 Fig. 10 shows the model simulation of undrained triaxial compression tests with different initial
357 densities using the same set of parameters. It is observed that parameter c has significant impacts
358 on the stress-strain response (Fig. 10a) and the stress paths (Fig. 10b). Simulation with c = 1.0
359 gives more realistic response similar to the typical undrained behavior of sand. Specifically, the
360 initial contraction trend introduced by c permits the initial decrease of shear strength and leftward
361 shifting of effective stress path upon shearing, which are the signatures of undrained response of

362 sand. Of course, the initial leftward trend given by this preliminary model is a bit over predicted.
363 Such secondary feature can be addressed with refined evolution laws as will be shown in the next
364 section. All simulations reached the expected critical state line Eq. (14) at the end of shearing (Fig.
365 10c). The corresponding evolution of fabrics are plotted in Figs 10d-f. The deviatoric fabric F
366 approached to different critical values (Figs 10d and e) because F_c is density-dependent. This can
367 be better inspected through Fig. 10f. One can see that the fabric paths under undrained shear
368 condition are predicted to be vertical lines approaching to the critical fabric surface. This is because
369 the current model adopts a one-to-one relation between Δ and ϕ where both are constants in
370 undrained case. This result contradicts with experiments as alternations of coordination number
371 has been observed in DEM simulations of undrained tests. We believe that this can be fixed by
372 introducing the dependency of F in Eq. (13) which is currently pursued in a separate study.

373 Fig. 11 presents model predictions of cyclic oedometer tests for the case of e=0.85. First of all, the
374 model gives a reasonable K_0 consolidation line in the p-q space (Fig. 11b). Sensitivity analyses
375 (which is not shown here due to space limitation) reveals that the slope of the K_0-line is affected
376 by both elastic and hardening parameters. Increase of b and c and decrease of a, G_0 and ν give
377 steeper slope of this line in the stress space. Secondly, it is interesting to see that for a model with
378 a cone-shaped yield surface (i.e. without a cap) can actually capture the cyclic densification (or
379 ratcheting) effect under oedometric condition. This is because that the stress path of cyclic
380 oedometer test is not strictly a line that within the cone but moves between the upper and lower
381 yield surfaces as loading-unloading occurs. During each loading cycle, the introduction of c gives
382 the model the ability to simulate densification even for initial states denser than critical (Fig. 11a).
383 Such densification effect ceases as the number of cycles accumulates. The terminal void ratio is
384 determined by parameter c with higher values of c give stronger ratcheting effect and lower

ultimate void ratio. When setting c=0, the ultimate void ratio coincides with the critical state void ratio which will cause cyclic loosening for dense specimens. The ability for the model to capture ratchetting is granted by the Δ evolution law Eq. (28). For either dense or loose sand, the second term of Eq. (28) generates a positive increment of Δ whenever loading reversal occurs. Cyclic loading will thus bring the state to the dense side (i.e. $\Delta > \Delta_c$). This makes the first term of Eq. (28) negative and provides compensating mechanism to slow down the speed of densification. After many cycles, the effects of the first and the second terms eventually reach to a dynamic equilibrium, resulting in the net effect of $d\Delta^p = 0$ and the cease of densification.

One more interesting observation from Figs 11b and c is that the model predicts a decrease of q and F with increasing number of cycles. This implies that cyclic loading tends to mitigate the initial anisotropy developed during the first K_0 loading which can eventually lead to the regain of an isotropic state. Such restoration occurs faster for samples exhibit low ratchetting than the opposite. This is not necessarily counter-intuitive as we know samples prepared by moist/dry tamping which involves repeated vertical impacts is much less anisotropic compared to those prepared by wet/dry pluviation method (Wan and Guo, 2001).

Figs. 12a-c presents simulations of isotropically consolidated undrained cyclic triaxial tests on dense and loose specimens with fixed cyclic stress ratio ($CSR = \Delta\sigma_a / 2\sigma_r = 0.05$). It is observed that the model successfully captures the typical undrained response of sand, including 1) liquefaction induced by cyclic loading, 2) the "butterfly" pattern of the stress path near p=0 (Fig. 12a), and the "banana" pattern of the stress-strain curve near liquefaction (Fig. 12b). Specimens with lower initial void ratio (i.e. e=0.7) is predicted to have reduced liquefaction potential reflected through the cease of p reduction after many cycles of shear loading (Figs 12a and b). The evolution of fabric anisotropy is small at beginning before liquefaction. As the number of cycles increase,

408 the fabric state approaches to the critical fabric surface on the p-F plane and the magnitude of F
409 changes become amplified (Fig. 12c). This trend has been exactly observed in the recent DEM
410 study by Wang, Fu, Zhang and Dafalias (2016). Cyclic loading after liquefaction is predicted to
411 be accompanied by drastic changes of fabric anisotropy (Fig. 12d).

412 Fig 13a presents the undrained cyclic test with varying cyclic stress ratio. The model correctly
413 captures the decreased number of loading cycles to reach liquefaction with increased shear stress,
414 which coincides with typical undrained cyclic behavior of sand. The results can be also presented
415 in terms of CSR vs. number of cycles to initiate liquefaction, as shown in Fig. 13b.

416 In summary, the basic model has demonstrated its capability in capturing the first-order behavior
417 of sand under monotonic, cyclic, drained and undrained loading paths. So far, the model only
418 contains three fitting parameters (i.e. a, b, and c) that governs the evolution of fabric. The rest of
419 the parameters all have clear physical meanings and can be calibrated by independent experiments.
420 This basic framework can be readily extended to produce more realistic prediction of the quasi-
421 static behavior of sand.

422 **ENHANCED FABRIC EVOLUTION LAWS**

423 Fig. 10b showed that the basic model over predicts the leftward shifting of stress path at beginning
424 of undrained shearing. Common experimental observation is that the initial stress path is almost
425 perpendicular to the p-axis and they only start to deviate at higher stress-ratios for specimens with
426 different densities. Changing parameter c only alters the initial slope of the leftward trend but not
427 the overall shape. This is because the rate of deviatoric fabric evolution Eq. (30) (and hence the
428 development of deviatoric stress) is always proportional to the rate of contraction controlled by
429 the second term of Eq. (28) (and hence the reduction of effective stress) in the basic model. To

remediate, some nonlinearity should be introduced in Eq. (30) allow control over the shape of the undrained stress path, i.e.:

$$dF_{ij} = \lambda b \exp\left(k_1 \left\| F_{ij}^c - F_{ij} \right\|\right)\left(F_{ij}^c - F_{ij}\right) \tag{32}$$

where k_1 is a new parameter. Fig. 14 shows the predicted undrained stress path and stress strain response using Eq. (32). It is observed that the shape of stress path is significantly improved with k_1 controlling the initial slope as well as maintaining the 'elbow' shape at higher stress ratios (Fig. 14a). Increased k_1 also has the effect of elevating the location of the first stress plateau on the stress-strain curve (Fig. 14b).

The basic model already has the capability to predict pressure- and density- dependent stress-strain-fabric behavior as demonstrated in Figs. 8-13. Such dependency is however only controlled by the shape of the critical fabric surface via Δ_c and F_{ij}^c, which is not enough to capture the pressure and density dependency of real soils. Here two more factors are introduced to scale parameters b and c with respect to density. The final fabric evolution laws for the enhanced model are given by

$$dF_{ij} = \lambda b \exp\left(k_2\left(\Delta - \Delta_0\right)\right)\exp\left(k_1 \left\| F_{ij}^c - F_{ij} \right\|\right)\left(F_{ij}^c - F_{ij}\right) \tag{33}$$

$$d\Delta^p = \lambda\left[a\left(\Delta_c - \Delta\right) + c\exp\left(k_3\left(\Delta - \Delta_0\right)\right)\left\| F_{ij}^c - F_{ij} \right\|\right] \tag{34}$$

where k_2 and k_3 are new parameters controlling the density-dependent evolution of F and Δ, respectively. In total, there are 6 parameters controlling fabric evolution, with a, b and c inherited from the basic model and k_1, k_2 and k_3 added in this enhancement.

449 The undrained triaxial test data by Verdugo and Ishihara (1996) on Toyoura sand is used here to
450 examine the performance of the enhanced model. Since the data shown in Fig. 6 is from the same
451 experiment, the calibrated critical state parameters are kept the same. Dafalias and Manzari (2004)
452 showed that the elastic parameters G_0=125 and ν=0.05 works well for this set of data. The
453 remaining 6 fabric evolution parameters are calibrated to best match the experimental stress path
454 and stress-strain curves. The model parameters are summarized Table 2.

455 Fig. 15 presents the simulation and the experimental results. A satisfactory agreement is observed
456 for a wide range of confining stresses (i.e. p_c=0.1~3 MPa) and initial void ratios (i.e.
457 e_0=0.735~0.907). It shows that the model is versatile enough to offer quantitative match on both
458 stress path and stress-strain curves at different stress and density levels for natural sand. Comparing
459 to classical critical-state models, the proposed model provides additional predictions on the
460 evolution of fabric anisotropy and coordination number, as shown in Fig. 16. It is observed that
461 the specimens with the same initial void ratio have their deviatoric fabrics evolve towards the same
462 critical value given by Eq. (10) (Fig. 16a). The effect of confining pressure on the evolution of F
463 is insignificant according to the current evolution equations (Fig. 16b).

464 **DISCUSSIONS AND CONCLUSIONS**

465 We started by reviewing the recent DEM and experimental findings on microstructural evolution
466 of granular soils subjected to quasi-static shearing. This survey highlights that the deviator of the
467 strong-contact fabric tensor seems to obey a simple linear relation with the stress deviator and
468 exhibits a critical surface similar to the critical stress surface on the π-plane. Synthesizing these
469 results leads to a new interpretation of the critical state conditions for granular soils. The central
470 idea is the existence of an ultimate critical fabric surface that attracts the fabric states upon shearing.
471 Additional model elements including a fabric-stress relation, a fabric-porosity relation and fabric

evolution laws are then built revolving around this core. The classical critical state conditions on stress ratio and void ratio are shown to be automatically satisfied in this framework.

The proposed theory and the Anisotropic Critical State Theory (ACST) by Li and Dafalias (2012) have some similarities and marked differences. Both theories describe the same phenomenon and emphasizes the role of fabric on the critical state. The difference is that ACST requires three critical-state attractors, the *M*-line in the *p*-*q* space, the critical state line in the *e*-*p* space and the $\hat{F}_{ij}^{c}$ envelop in the normalized deviatoric fabric space, and all three conditions must be satisfied at critical state. On the contrary, the proposed theory only requires a single critical-state attractor, that is the critical fabric surface. All other apparent critical states such as the CSL in the *e*-*p*-*q* space are consequences of the fabric tensor approaching to its critical value. The simultaneous arrival of $G_{ij} = G_{ij}^{c}$ and the other apparent critical states is guaranteed by the secondary relations such as the fabric-stress and fabric-porosity relations. This alternative perspective on critical state has several advantages: 1) it unifies the various newly discovered critical-state conditions as discussed in the literature review section; 2) by defining a single attractor instead of keep adding different critical state conditions in various spaces, it offers a simpler and more structured framework for modeling granular soils; 3) fabric is no longer an add-on component to conventional elastoplastic models but rather the only vehicle that links the strain and the stress, which is physically plausible considering the micromechanical origin of stress and strain.

Following this idea, a new constitutive model is developed in this paper, where the mean and the deviatoric components of the fabric tensor (not the normalized fabric tensor) serve as the fundamental internal state variables of the model. The expressions of the critical fabric surface, the fabric-stress relation and Δ-ϕ relation are inspired from DEM results. Two sets of fabric

494 evolutions laws are proposed. One is relatively basic which is suitable to demonstrate the working
495 mechanisms of the model. The other set aims to capture the realistic behavior of granular soils.
496 With similar number of parameters compared to classical critical-state based models, the enhanced
497 model is able to capture the undrained response of Toyoura sand under wide range of pressure and
498 density conditions. Moreover, the model offers insights on the evolution of the mean and deviatoric
499 fabric during shearing. It is therefore concluded that the proposed theory provides an innovative
500 way to integrate microstructure information in the continuum modeling of granular soils.

501 Despite these promising results, the current study is still of exploratory nature. More DEM and
502 experimental data are needed to confirm several assumptions in this theory and provide more
503 accurate constitutive relations. First of all, it should be noted that the current work relies on fabric
504 tensor defined on the strong contact network. Generalization of the model to other fabric
505 definitions requires extensive additional research. As shown in Fig. 2b, the total-contact fabric
506 ratio and stress ratio does not obey a simple linear relationship and is shear-mode dependent. In
507 this case, the fabric-stress relation seems to be more suitably described in an incremental form
508 rather than the total form like Eq. (2). One obvious consequence of such an incremental relation is
509 that a deviatoric stress state can correspond to multiple anisotropic fabric states depending on the
510 loading history. This is perhaps more physical as one can achieve a soil specimen with the same
511 stress and void ratio but different degree of initial anisotropy, enabling much richer predictive
512 capability of the model. Regardless, how such incremental fabric-stress relation alters the
513 mathematical structure of the model demands further investigation. Secondly, the assumption that
514 porosity only depends on the mean part of the fabric tensor Δ is not accurate for granular soils
515 subjected to shearing as discussed before. An immediate follow-up study is to seek for a $\phi(\Delta, F_{ij})$
516 relation supported by DEM data for more realistic prediction of the fabric paths under constant ϕ

517 (i.e. undrained) loading conditions. It is however expected that incorporating a $\phi(\Delta, F_{ij})$ relation
518 instead of the current $\phi(\Delta)$ relation will still produce a unique critical void ratio at critical state
519 given that both Δ and F_{ij} are attracted by the critical fabric surface.

520 **DATA AVAILABILITY**

521 Some or all data, models, or code generated or used during the study are available from the
522 corresponding author by request.

523 **ACKNOWLEDGEMENT**

524 Yida Zhang wishes to express thanks for the start-up fund provided by the Department of Civil,
525 Environmental and Architectural Engineering at the University of Colorado Boulder, USA.

526 **REFERENCES**

527 Arakawa, M., and Nishino, M. (1973). "Coordination number in a random mixtures of hard
528 spheres." *Journal of the Society of Material Science, Japan*, 22, 658.
529 Bernal, J. D. (1960). "Geometry of the structure of monatomic liquids." *Nature*, 185(4706), 68-70.
530 Calvetti, F., Combe, G., and Lanier, J. (1997). "Experimental micromechanical analysis of a 2D
531 granular material: relation between structure evolution and loading path." *Mechanics of*
532 *Cohesive-frictional Materials: An International Journal on Experiments, Modelling and*
533 *Computation of Materials and Structures*, 2(2), 121-163.
534 Cowin, S. C. (1985). "The relationship between the elasticity tensor and the fabric tensor."
535 *Mechanics of Materials*, 4(2), 137-147.
536 Dafalias, Y. F., and Manzari, M. T. (2004). "Simple plasticity sand model accounting for fabric
537 change effects." *Journal of Engineering mechanics*, 130(6), 622-634.

Dafalias, Y. F., and Taiebat, M. (2016). "SANISAND-Z: zero elastic range sand plasticity model." *Géotechnique*, 66(12), 999-1013.

Dodds, J. (1980). "The porosity and contact points in multicomponent random sphere packings calculated by a simple statistical geometric model." *Journal of colloid and interface science*, 77(2), 317-327.

Fu, P., and Dafalias, Y. F. (2011). "Fabric evolution within shear bands of granular materials and its relation to critical state theory." *International Journal for numerical and analytical methods in geomechanics*, 35(18), 1918-1948.

Fu, P., and Dafalias, Y. F. (2015). "Relationship between void-and contact normal-based fabric tensors for 2D idealized granular materials." *International Journal of Solids and Structures*, 63, 68-81.

German, R. M. (2014). "Coordination number changes during powder densification." *Powder Technology*, 253, 368-376.

Imseeh, W. H., Druckrey, A. M., and Alshibli, K. A. (2018). "3D experimental quantification of fabric and fabric evolution of sheared granular materials using synchrotron micro-computed tomography." *Granular Matter*, 20(2), 24.

Kanatani, K.-I. (1984). "Distribution of directional data and fabric tensors." *International Journal of Engineering Science*, 22(2), 149-164.

Kruyt, N. P. (2012). "Micromechanical study of fabric evolution in quasi-static deformation of granular materials." *Mechanics of materials*, 44, 120-129.

Kruyt, N. P., and Rothenburg, L. (2014). "On micromechanical characteristics of the critical state of two-dimensional granular materials." *Acta mechanica*, 225(8), 2301-2318.

Li, X., and Dafalias, Y. (2015). "Dissipation consistent fabric tensor definition from DEM to continuum for granular media." *Journal of the Mechanics and Physics of Solids*, 78, 141-153.

Li, X. S., and Dafalias, Y. F. (2012). "Anisotropic critical state theory: role of fabric." *Journal of Engineering Mechanics*, 138(3), 263-275.

Li, X. S., and Wang, Y. (1998). "Linear representation of steady-state line for sand." *Journal of Geotechnical and Geoenvironmental Engineering*, 124(12), 1215-1217.

Mooney, M. A., Finno, R. J., and Viggiani, M. G. (1998). "A unique critical state for sand?" *Journal of Geotechnical and Geoenvironmental Engineering*, 124(11), 1100-1108.

Nguyen, H., Rahman, M., and Fourie, A. (2016). "Undrained behaviour of granular material and the role of fabric in isotropic and K 0 consolidations: DEM approach." *Géotechnique*, 67(2), 153-167.

Nguyen, H., Rahman, M., and Fourie, A. (2018). "Characteristic Behavior of Drained and Undrained Triaxial Compression Tests: DEM Study." *Journal of Geotechnical and Geoenvironmental Engineering*, 144(9), 04018060.

O'hern, C. S., Silbert, L. E., Liu, A. J., and Nagel, S. R. (2003). "Jamming at zero temperature and zero applied stress: The epitome of disorder." *Physical Review E*, 68(1), 011306.

Oda, M. (1972a). "Deformation mechanism of sand in triaxial compression tests." *Soils and Foundations*, 12(4), 45-63.

Oda, M. (1972b). "The mechanism of fabric changes during compressional deformation of sand." *Soils and foundations*, 12(2), 1-18.

Oda, M. (1977). "Co-ordination number and its relation to shear strength of granular material." *Soils and foundations*, 17(2), 29-42.

582 Ouchiyama, N., and Tanaka, T. (1984). "Porosity estimation for random packings of spherical
583 particles." *Industrial & engineering chemistry fundamentals*, 23(4), 490-493.
584 Papadimitriou, A. G., Chaloulos, Y. K., and Dafalias, Y. F. (2019). "A fabric-based sand plasticity
585 model with reversal surfaces within anisotropic critical state theory." *Acta Geotechnica*,
586 14(2), 253-277.
587 Radjai, F., Delenne, J.-Y., Azéma, E., and Roux, S. (2012). "Fabric evolution and accessible
588 geometrical states in granular materials." *Granular Matter*, 14(2), 259-264.
589 Radjai, F., Jean, M., Moreau, J.-J., and Roux, S. (1996). "Force distributions in dense two-
590 dimensional granular systems." *Physical review letters*, 77(2), 274.
591 Rice, R. W. (1993). "Evaluating porosity parameters for porosity–property relations." *Journal of*
592 *the American Ceramic Society*, 76(7), 1801-1808.
593 Roscoe, K. H., Schofield, A., and Wroth, C. (1958). "On the yielding of soils." *Geotechnique*,
594 8(1), 22-53.
595 Rothenburg, L., and Kruyt, N. P. (2004). "Critical state and evolution of coordination number in
596 simulated granular materials." *International Journal of Solids and Structures*, 41(21), 5763-
597 5774.
598 Schofield, A., and Wroth, P. (1968). "Critical state soil mechanics."
599 Shi, J., and Guo, P. (2018). "Fabric evolution of granular materials along imposed stress paths."
600 *Acta Geotechnica*, 13(6), 1341-1354.
601 Smith, W. O., Foote, P. D., and Busang, P. F. (1929). "Packing of homogeneous spheres." *Physical*
602 *Review*, 34(9), 1271.

603 Suzuki, M., Kada, H., and Hirota, M. (1999). "Effect of size distribution on the relation between
604 coordination number and void fraction of spheres in a randomly packed bed." *Advanced*
605 *Powder Technology*, 10(4), 353-365.
606 Tasiopoulou, P., and Gerolymos, N. (2016). "Constitutive modelling of sand: a progressive
607 calibration procedure accounting for intrinsic and stress-induced anisotropy." *Géotechnique*,
608 66(9), 754-770.
609 Thornton, C., and Zhang, L. (2010). "On the evolution of stress and microstructure during general
610 3D deviatoric straining of granular media." *Géotechnique*, 60(5), 333-341.
611 Vaid, Y., and Thomas, J. (1995). "Liquefaction and postliquefaction behavior of sand." *Journal*
612 *of Geotechnical Engineering*, 121(2), 163-173.
613 Verdugo, R., and Ishihara, K. (1996). "The steady state of sandy soils." *Soils and foundations*,
614 36(2), 81-91.
615 Wan, R., and Guo, P. (2001). "Effect of microstructure on undrained behaviour of sands."
616 *Canadian Geotechnical Journal*, 38(1), 16-28.
617 Wang, G., and Wei, J. (2016). "Microstructure evolution of granular soils in cyclic mobility and
618 post-liquefaction process." *Granular Matter*, 18(3), 51.
619 Wang, R., Fu, P., Zhang, J.-M., and Dafalias, Y. F. (2016). "DEM study of fabric features
620 governing undrained post-liquefaction shear deformation of sand." *Acta Geotechnica*, 11(6),
621 1321-1337.
622 Wang, R., Fu, P., Zhang, J.-M., and Dafalias, Y. F. (2017). "Evolution of various fabric tensors
623 for granular media toward the critical state." *Journal of Engineering Mechanics*, 143(10),
624 04017117.

625 Wiebicke, M., Andò, E., Salvatore, E., Viggiani, G., and Herle, I. "Experimental measurement of
626 granular fabric and its evolution under shearing." *Proc., EPJ Web of Conferences*, EDP
627 Sciences, 02020.
628 Yan, W., and Zhang, L. (2013). "Fabric and the critical state of idealized granular assemblages
629 subject to biaxial shear." *Computers and Geotechnics*, 49, 43-52.
630 Yang, R., Zou, R., and Yu, A. (2000). "Computer simulation of the packing of fine particles."
631 *Physical Review E*, 62(3), 3900.
632 Yang, Z., and Wu, Y. (2016). "Critical state for anisotropic granular materials: a discrete element
633 perspective." *International Journal of Geomechanics*, 17(2), 04016054.
634 Yoshimine, M., Ishihara, K., and Vargas, W. (1998). "Effects of principal stress direction and
635 intermediate principal stress on undrained shear behavior of sand." *Soils and Foundations*,
636 38(3), 179-188.
637 Zhao, J., and Gao, Z. (2015). "Unified anisotropic elastoplastic model for sand." *Journal of*
638 *Engineering Mechanics*, 142(1), 04015056.
639 Zhao, J., and Guo, N. (2013). "Unique critical state characteristics in granular media considering
640 fabric anisotropy." *Géotechnique*, 63(8), 695.
641

List of Tables and Figures

Table 1: Triaxial equations of the basic model

Table 2: Model parameters for Toyoura sand

Fig. 1: Critical fabric line observed in a) 2D DEM simulations (replotted from Kruyt and Rothenburg (2014)), b) 2D DEM simulation using elongated particles (replotted from Fu and Dafalias (2011)), c) 3D DEM simulations (replotted from Nguyen et al. (2018)). In above figures, $A=\hat{G}_1-\hat{G}_3$ is the deviatoric fabric; $\hat{G}$ is the normalized fabric tensor of the first kind; subscripts 1, 2 and 3 denote the major, intermediate and minor principal values, respectively.

Fig. 2: a) Results from Oda (1972a); b) stress ratio vs. total-contact based fabric ratio; c) stress ratio vs. strong-contract based fabric ratio; d) critical-state stress and fabric envelops in the deviatoric plane (b,c,d modified from Shi and Guo (2018))

Fig. 3: Critical fabric surface in a) principal space, b) p-Δ-F space and c) p-Δ-$\hat{F}$ space. Parameters used in this Fig.: $\hat{F}_c$=1.2, r=0.8, Δ_{c0}=3.91, h_c=0.36, p_a=100kPa, ξ=0.55. The last four parameters are directly taken from Nguyen et al. (2018).

Fig. 4: Eq. **Error! Reference source not found.** vs. experimental data a) for mono-sized granular assembly and b) for bi- and multi- mixed assemblies. The early experimental in a) are extracted from Ouchiyama and Tanaka (1981) who referred to Arakawa and Nishino (1973), Bernal (1960) and Smith et al. (1929) .

Fig. 5: CSL data of Toyoura sand from Verdugo and Ishihara (1996) interpreted by Eq. **Error! Reference source not found.** and Li and Wang (1998)'s equation. Parameters used: Δ_0=2; ϕ_0= 0.4942; h_0=20; ζ=1.5; Δ_{c0}=2.027; h_c= 0.0129; ξ=0.98.

Fig. 6: a) Critical fabric surface and an arbitrary fabric state A; b) Yield surface corresponding to the fabric state A. Parameters used: $\hat{F}_c$=1.2, r=0.8, m=0.05.

Fig. 7: Model vs. experimentally observed critical fabric and stress surfaces. Data from Shi and Guo (2018). Parameters used: $\hat{F}_c$=1.8, r=0.9.

Fig. 8: Model results of drained triaxial compression test. In figures c and f, cross symbol indicates the initial states and cycle symbol represents the critical states achieved at ε_a=0.5. Dotted line represents critical state line.

Fig. 9: Drained triaxial compression results from 2D DEM simulations by Rothenburg and Kruyt (2004).

Fig. 10: Model results of undrained triaxial compression test. In figures c and f, cross symbol indicates the initial states and cycle symbol represents the critical states achieved at ε_a=0.5. Dotted line represents critical state line.

Fig. 11: Cyclic oedometer tests to show the ratcheting effect. Dotted line represents critical state line.

Fig. 12: Model results of undrained cyclic triaxial tests with fixed CSR. All simulations are conducted using c=0.5. Dotted line represents critical state line.

Fig. 13: a) Model results of undrained cyclic triaxial tests with varying CSR for e=0.8 sand. b) liquefaction potential predicted by the model. All simulations are conducted using *c*=0.5. Dotted line represents critical state line.

Fig. 14: Effect of k_1 on the shape of undrained stress path for e=0.8 and c=1. The rest of the parameters are identical to Fig. 11.

Fig. 15: Simulations vs. experiments in undrained compression tests on Toyoura sand. Data from Verdugo and Ishihara (1996).

Fig. 16: The predicted fabric evolution corresponding to Verdugo and Ishihara's experiment.

Table 1: Triaxial equations of the basic model

Model components	Equations
Elasticity	$p = K\varepsilon_v^e; \quad q = 3G\varepsilon_s^e$
Critical fabric surface	$F_c = \hat{F}_c \,\mathrm{sgn}(\eta-\alpha)\Delta_c; \quad \Delta_c = \Delta_{c0} + h_c\left(p/p_a\right)^{\xi}$
Yield surface	$y = \lvert\eta-\alpha\rvert - m = 0$
Fabric-stress relation	$\alpha = (2/5)\hat{F}$
Plasticity	$d\varepsilon_v^p = \left(\partial\varepsilon_v/\partial\Delta\right)d\Delta^p; \quad d\varepsilon_s^p = \lambda\,\mathrm{sgn}(\eta-\alpha)$
Fabric evolution	$d\Delta^e = \left(\partial\varepsilon_v/\partial\Delta\right)^{-1} d\varepsilon_v^e$
	$d\Delta^p = \lambda\left[a\left(\Delta_c-\Delta\right)+c\lvert F_c-F\rvert\right]$
	$dF = \lambda b\left(F_c-F\right)$

Table 2: Model parameters for Toyoura sand

Role	Notation	Value
Elasticity	G_0	125
	ν	0.05
Critical fabric	Δ_{c0}	2.027
	h_c	0.0129
	ξ	0.98
	$\hat{F}_c$	3.125
	r	1
Δ-ϕ relation	Δ_0	2
	ϕ_0	0.4942
	h_0	20
	ζ	1.5
Yield surface	m	0.01
Fabric evolution	a	16
	b	15
	c	0.4
	k_1	0.4
	k_2	2
	k_3	3

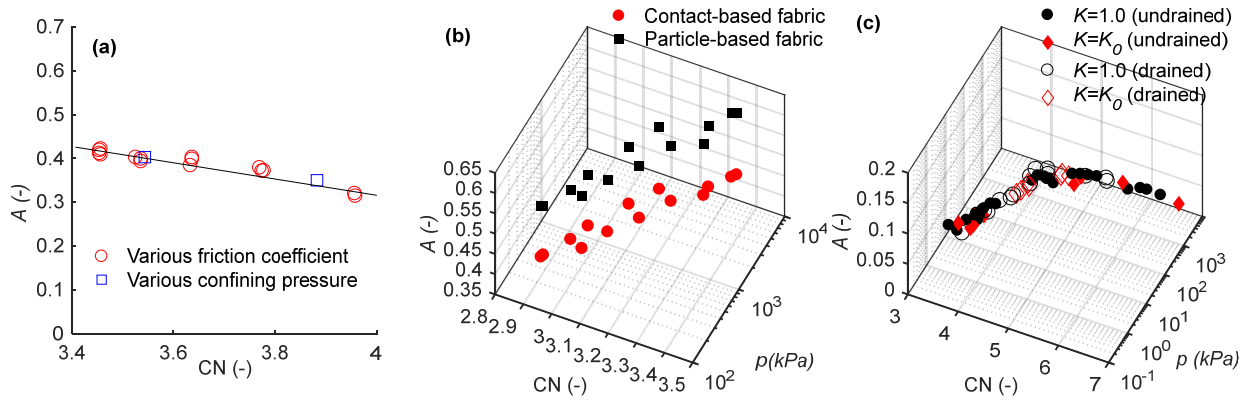

Fig. 1: Critical fabric line observed in a) 2D DEM simulations (replotted from Kruyt and Rothenburg (2014)), b) 2D DEM simulation using elongated particles (replotted from Fu and Dafalias (2011)), c) 3D DEM simulations (replotted from Nguyen et al. (2018)). In above figures, $A=\hat{G}_1-\hat{G}_3$ is the deviatoric fabric; $\hat{G}$ is the normalized fabric tensor of the first kind; subscripts 1, 2 and 3 denote the major, intermediate and minor principal values, respectively.

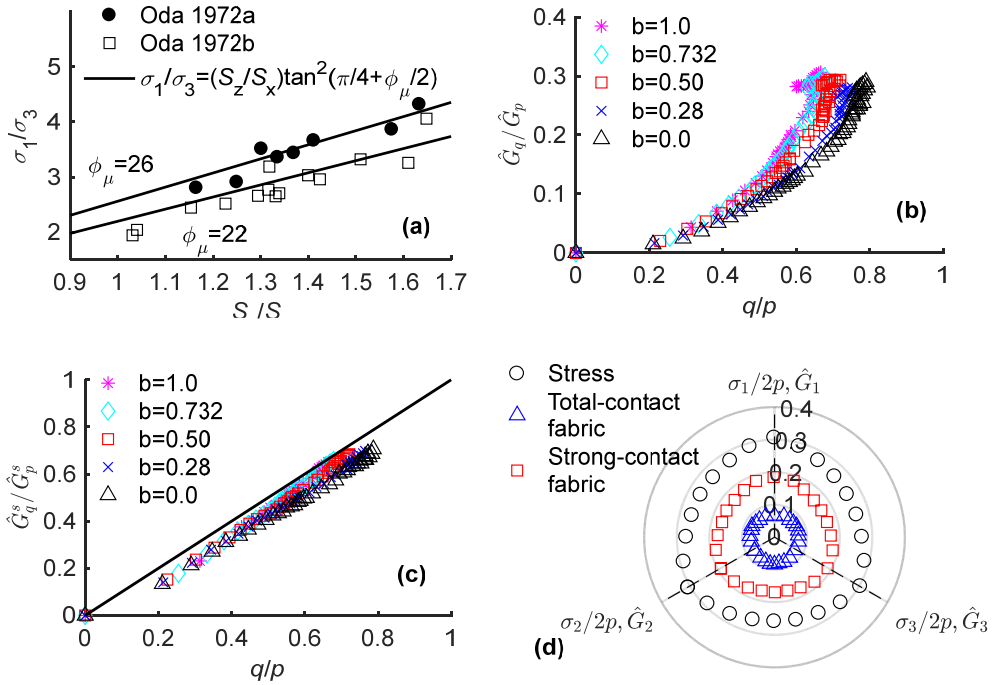

Fig. 2: a) Results from Oda (1972a); b) stress ratio vs. total-contact based fabric ratio; c) stress ratio vs. strong-contract based fabric ratio; d) critical-state stress and fabric envelops in the deviatoric plane (b,c,d modified from Shi and Guo (2018))

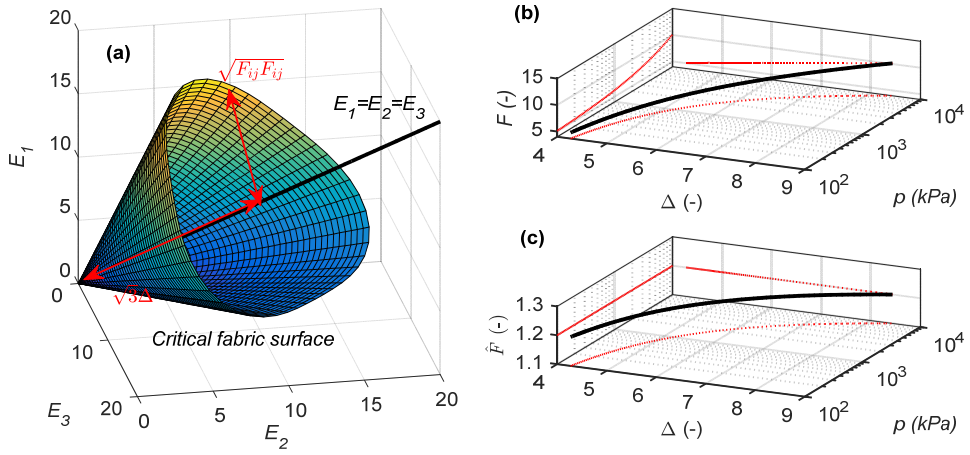

Fig. 3: Critical fabric surface in a) principal space, b) p-Δ-F space and c) p-Δ-$\hat{F}$ space. Parameters used in this Fig.: $\hat{F}_c$=1.2, r=0.8, Δ_{c0}=3.91, h_c=0.36, p_a=100kPa, ξ=0.55. The last four parameters are directly taken from Nguyen et al. (2018).

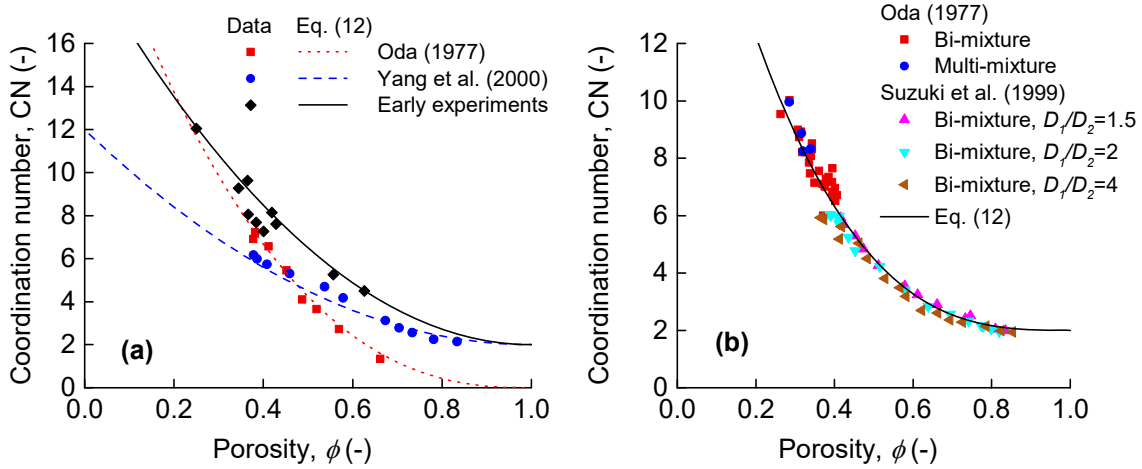

Fig. 4: Eq. **Error! Reference source not found.** vs. experimental data a) for mono-sized granular assembly and b) for bi- and multi- mixed assemblies. The early experimental in a) are extracted from Ouchiyama and Tanaka (1981) who referred to Arakawa and Nishino (1973), Bernal (1960) and Smith et al. (1929) .

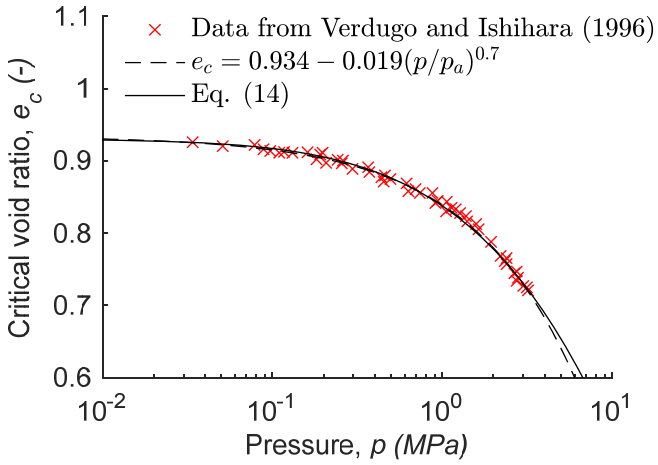

Fig. 5: CSL data of Toyoura sand from Verdugo and Ishihara (1996) interpreted by Eq. **Error! Reference source not found.** and Li and Wang (1998)'s equation. Parameters used: Δ_0=2; ϕ_0= 0.4942; h_0=20; ζ=1.5; Δ_{c0}=2.027; h_c= 0.0129; ξ=0.98.

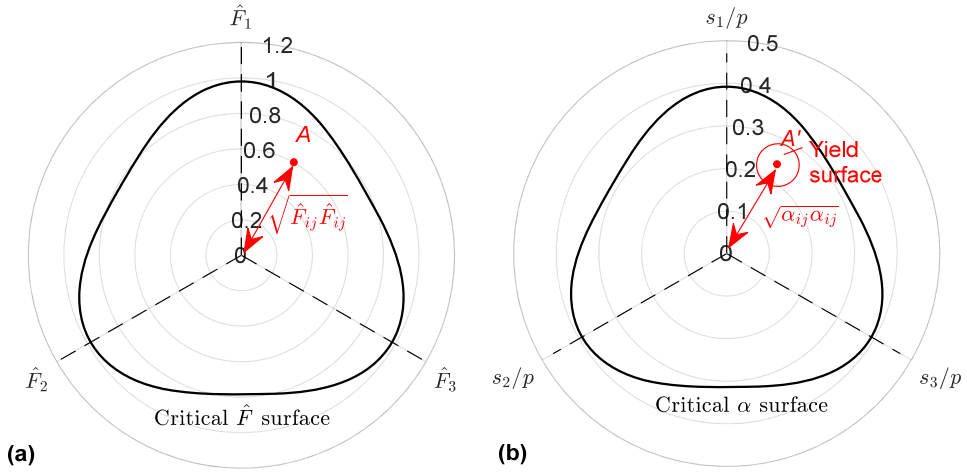

Fig. 6: a) Critical fabric surface and an arbitrary fabric state A; b) Yield surface corresponding to the fabric state A. Parameters used: $\hat{F}_c$=1.2, r=0.8, m=0.05.

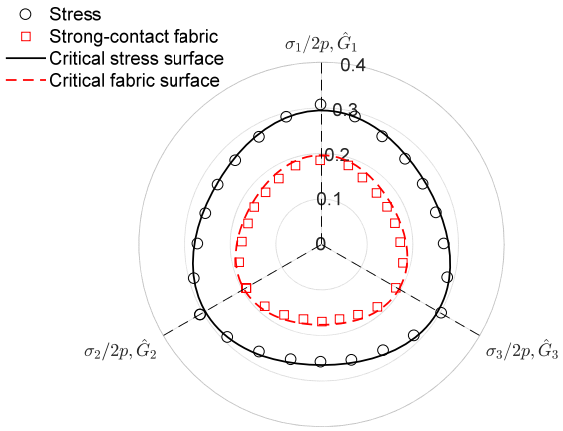

Fig. 7: Model vs. experimentally observed critical fabric and stress surfaces. Data from Shi and Guo (2018). Parameters used: $\hat{F}_c$=1.8, r=0.9.

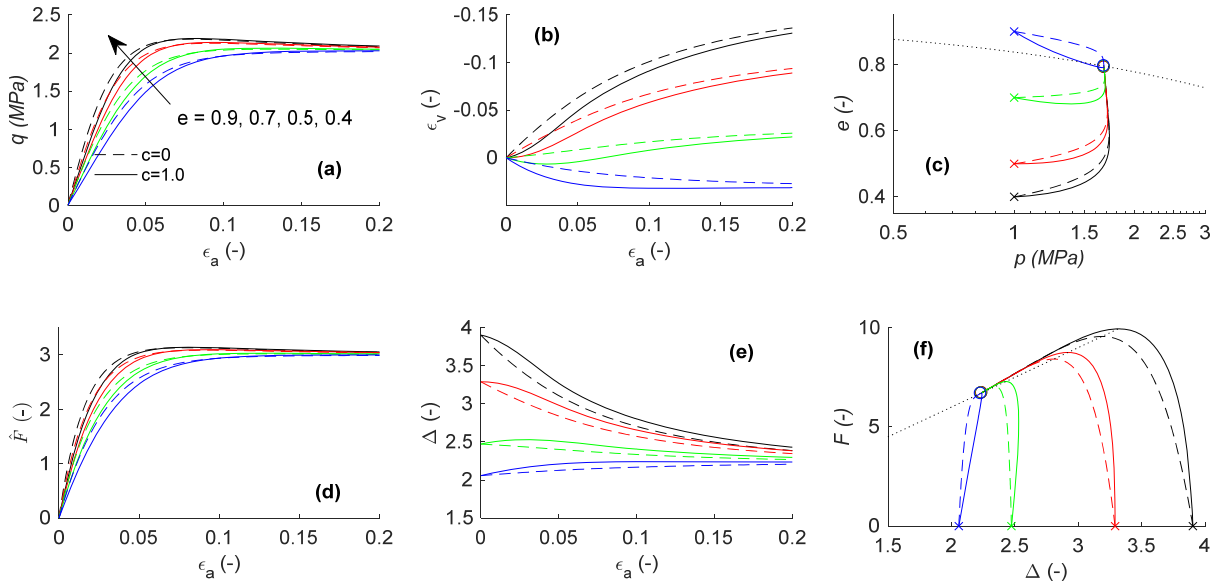

Fig. 8: Model results of drained triaxial compression test. In figures c and f, cross symbol indicates the initial states and cycle symbol represents the critical states achieved at ε_a=0.5. Dotted line represents critical state line.

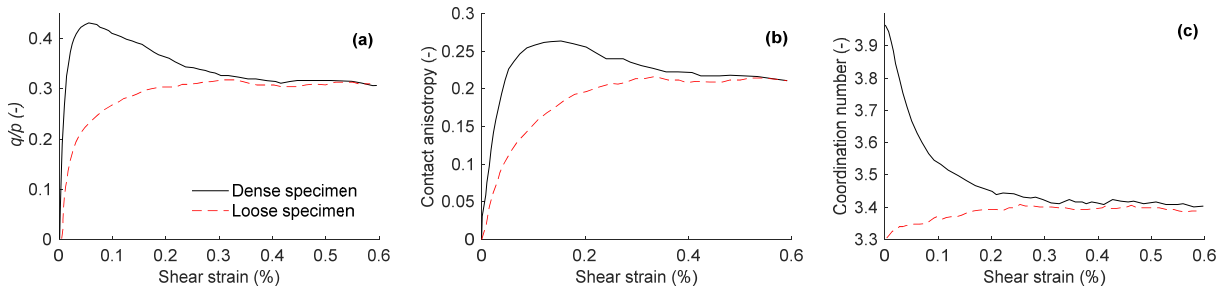

Fig. 9: Drained triaxial compression results from 2D DEM simulations by Rothenburg and Kruyt (2004).

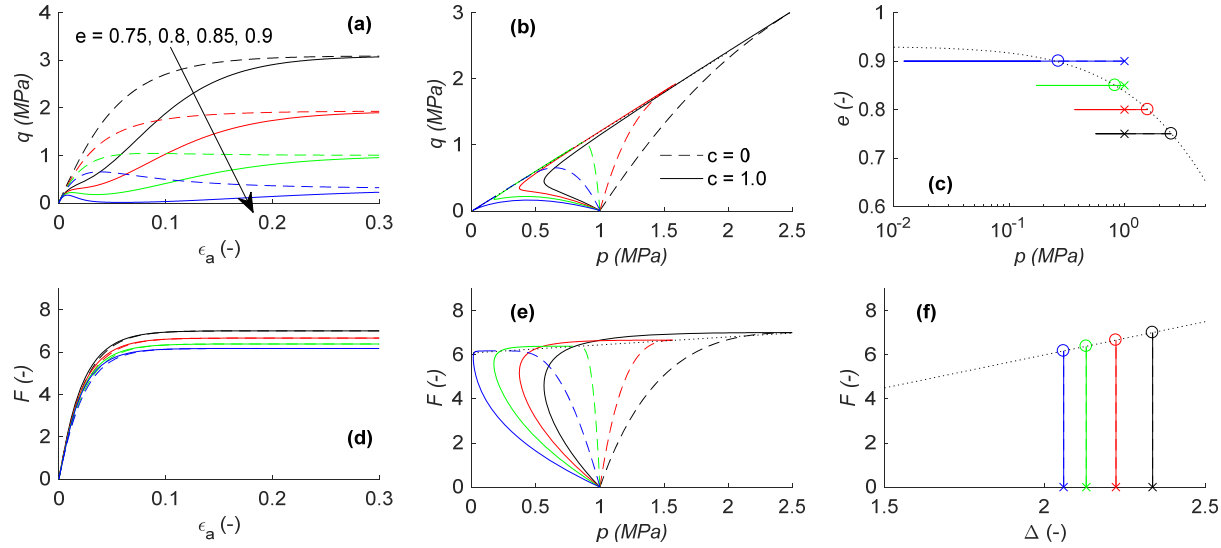

Fig. 10: Model results of undrained triaxial compression test. In figures c and f, cross symbol indicates the initial states and cycle symbol represents the critical states achieved at ε_a=0.5. Dotted line represents critical state line.

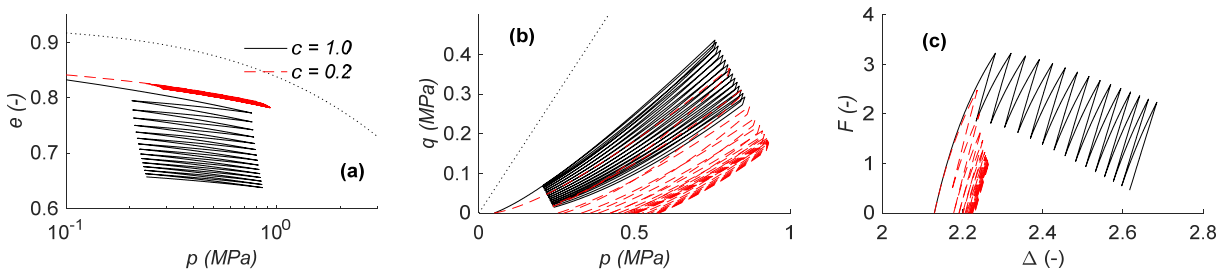

Fig. 11: Cyclic oedometer tests to show the ratcheting effect. Dotted line represents critical state line.

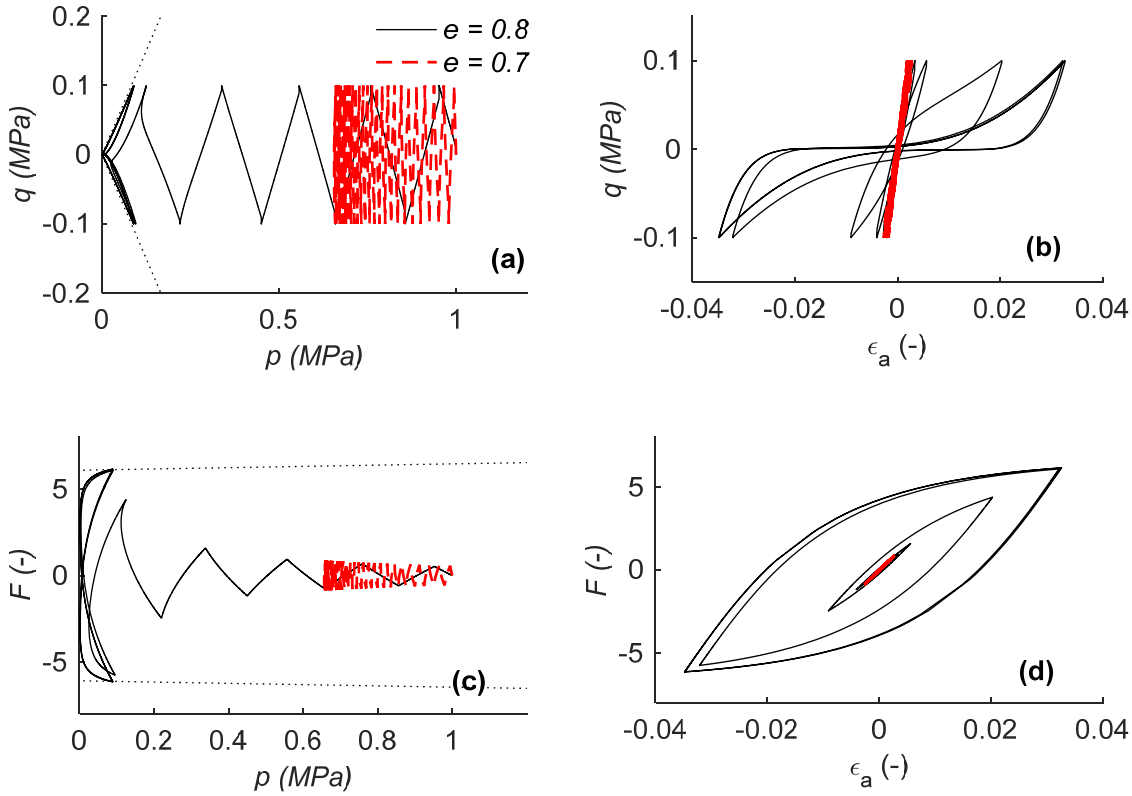

Fig. 12: Model results of undrained cyclic triaxial tests with fixed CSR. All simulations are conducted using c=0.5. Dotted line represents critical state line.

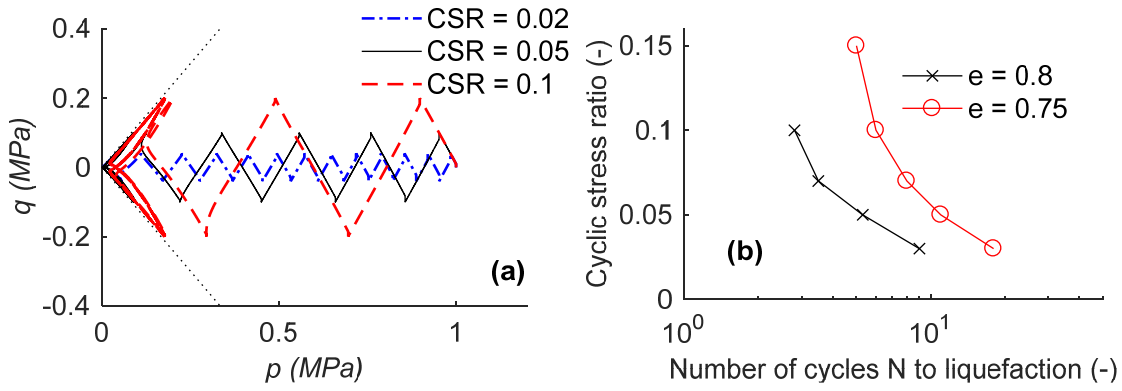

Fig. 13: a) Model results of undrained cyclic triaxial tests with varying CSR for e=0.8 sand. b) liquefaction potential predicted by the model. All simulations are conducted using *c*=0.5. Dotted line represents critical state line.

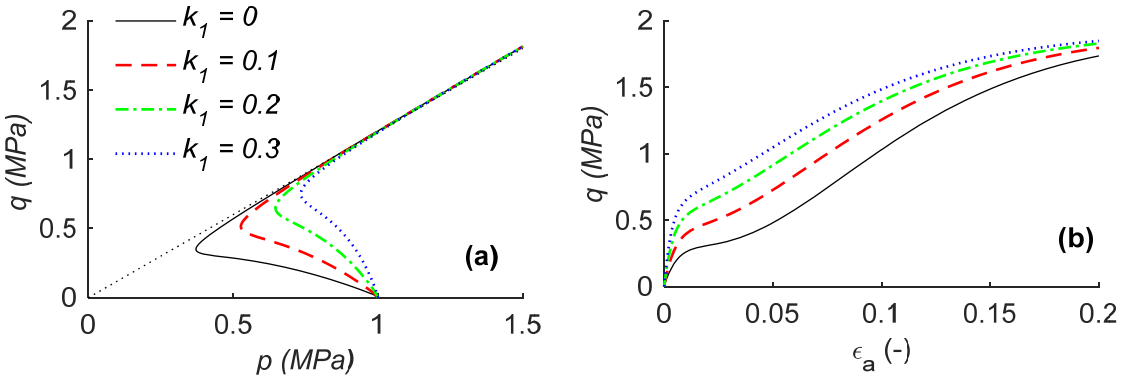

Fig. 14: Effect of k_1 on the shape of undrained stress path for e=0.8 and c=1. The rest of the parameters are identical to Fig. 11.

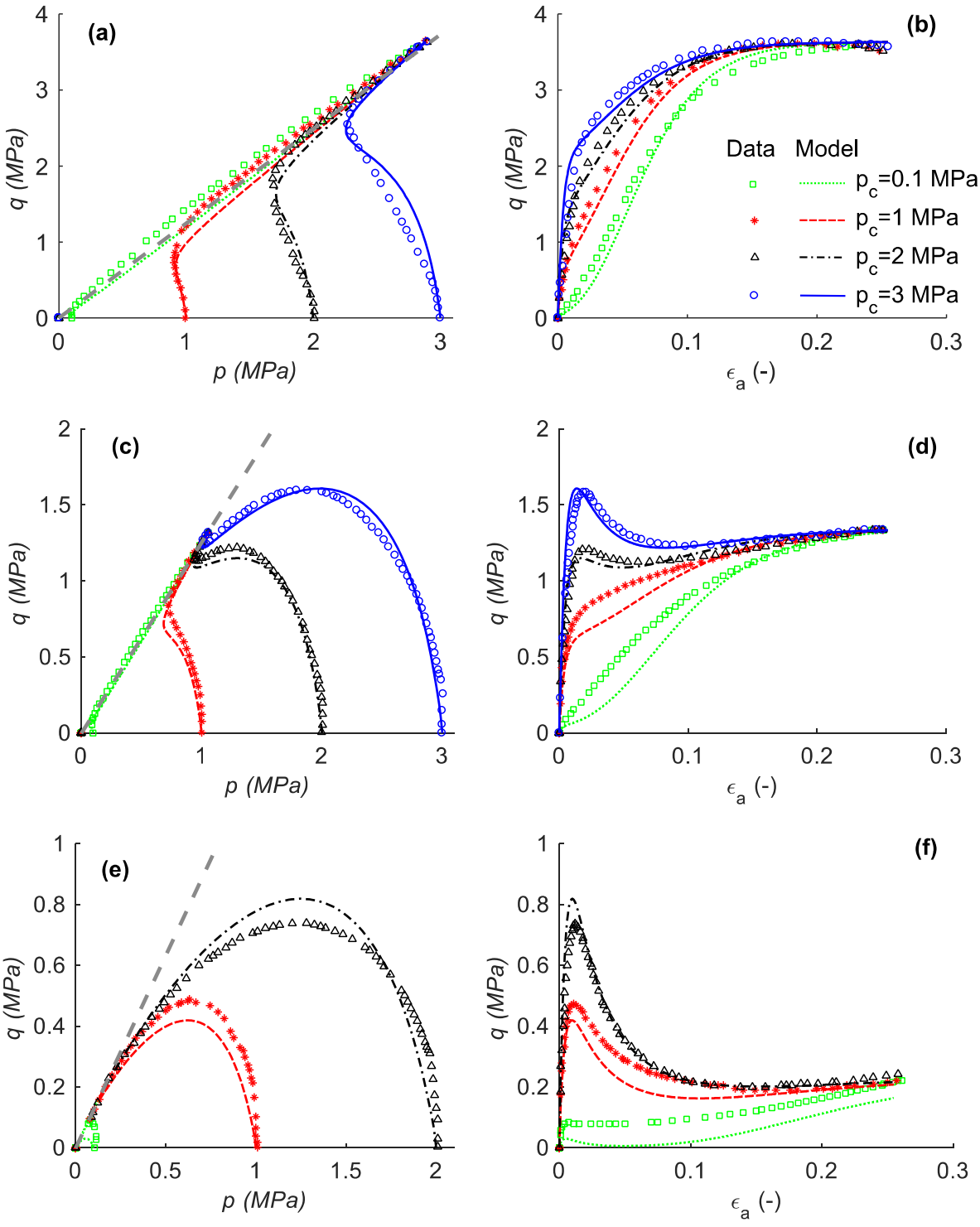

Fig. 15: Simulations vs. experiments in undrained compression tests on Toyoura sand. Data from Verdugo and Ishihara (1996).

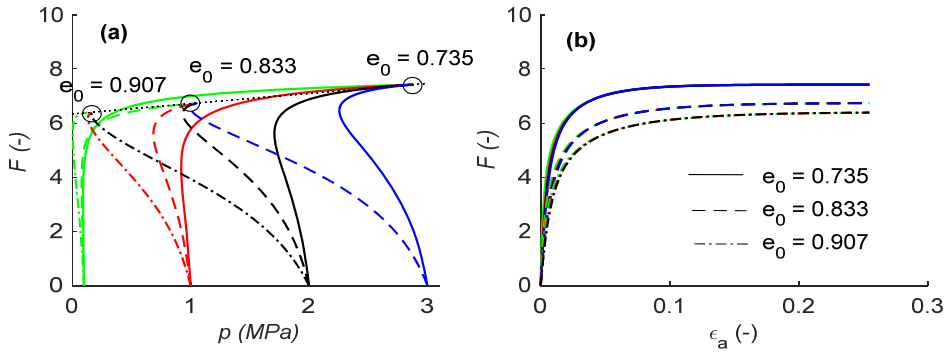

Fig. 16: The predicted fabric evolution corresponding to Verdugo and Ishihara's experiment.